

# Saturation of backward stimulated scattering of laser in kinetic regime: Wavefront bowing, trapped particle modulational instability and trapped particle self-focusing of plasma waves

L. Yin<sup>\*</sup>, B. J. Albright, K. J. Bowers<sup>†</sup>, W. Daughton, and H. A. Rose

*Los Alamos National Laboratory, Los Alamos, NM 87545.*

## Abstract

Backward stimulated Raman and Brillouin scattering (SRS and SBS) of laser are examined in the kinetic regime using particle-in-cell simulations. The SRS reflectivity measured as a function of the laser intensity in a single hot spot from two-dimensional (2D) simulations shows a sharp onset at a threshold laser intensity and a saturated level at higher intensities, as obtained previously in Trident experiments [D. S. Montgomery, et al., Phys. Plasmas, **9**, 2311, 2002]. In these simulations, wavefront bowing of electron plasma waves (ion acoustic waves) due to the trapped particle nonlinear frequency shift is observed in the SRS (SBS) regime for the first time, which increases with laser intensity. Self-focusing from trapped particle modulational instability (TPMI) [H. A. Rose, Phys. Plasmas, **12**, 12318, 2005] is shown to occur in both 2D and 3D SRS simulations. The key physics underlying nonlinear saturation of SRS is identified as a combination of wavefront bowing, TPMI and self-focusing: The wavefront bowing marks the beginning of SRS saturation

---

<sup>\*</sup>Email address: lyin@lanl.gov

<sup>†</sup>Guest Scientist. Currently with D. E. Shaw Research, LLC, New York, NY 10036.

and self-focusing terminates the SRS reflectivity, both effects resulting from cancellation of the source term for SRS. Ion acoustic wave bowing also contributes to the SRS saturation. Velocity diffusion by transverse modes and rapid loss of hot electrons in regions of small transverse extent formed from self-focusing lead to dissipation of the wave energy and an increase in the Landau damping rate in spite of strong electron trapping that reduces Landau damping initially. The ranges of wavelength and growth rate associated with transverse break-up of the EPW are also examined in 2D speckle simulations as well as in 2D periodic systems from BGK equilibrium and are compared with theory predictions.

52.35.Fp, 52.35.Mw, 52.38.Bv, 52.38.Dx



## I. INTRODUCTION

Laser-plasma interaction can involve two parametric instabilities: stimulated Raman scattering (SRS) and stimulated Brillouin scattering (SBS), where the laser light scatters off an electron-plasma (Langmuir) wave and an ion-acoustic wave (IAW), respectively. Mitigation and suppression of the growth of these instabilities is vital to the success of inertial confinement fusion (ICF) experiments at the National Ignition Facility (NIF) [1] and the laser Megajoule Facility (LMJ). To accomplish these important tasks, it is essential to understand the instability onset threshold and saturation. Motivated by recent experiments, we identify in this paper the key physics underlying nonlinear saturation of SRS and SBS in laser hot spots.

Intriguing results have been obtained from Trident single-hot spot experiments at LANL where SRS reflectivity was measured as a function of the laser intensity in an isolated single speckle [2,3]. A sharp onset at a threshold laser intensity and a saturated level of SRS at higher intensities have been obtained from these experiments at  $k\lambda_D = 0.33 - 0.35$  ( $k$  is the initial Langmuir wavenumber and  $\lambda_D$  is the plasma Debye length). It was shown that SRS reflectivity estimated from linear, spatial gain based on a steady-state model cannot account for the observed scaling. Similar features of rapid onset and saturation are also derived from one-dimensional (1D) particle-in-cell (PIC) simulations at  $k\lambda_D = 0.34$  [4,5], and at other  $k\lambda_D$  values ranging from 0.24 to 0.45 [6]. In these regimes, the onset intensity decreases with decreasing  $k\lambda_D$ , while the saturation level decreases with increasing  $k\lambda_D$ , a result that has important implications for SRS mitigation in ignition experiments.

With regard to SRS research, it is well known that electron trapping and nonlinear frequency shift of a Langmuir wave (LW) [7,8] play an important role in the kinetic regime. Saturation of SRS has been considered as due to the increased nonlinear Landau damping through the generation of hot electrons [9] by trapping, or detuning of parametric instability by nonlinear frequency shift of LWs [10]. Recent studies show that the electron-plasma waves generated in the SRS process dynamically evolve from the initial Langmuir mode to

the electron beam-acoustic modes (BAM) [4,5] from the presence of a beam component in the trapping-modified the electron distribution function and that the laser light essentially scatters off BAM in the nonlinear stage. The resulting linear response of the system allows for parametric coupling with a broad range of nonlinear frequency shifts, manifesting as spectral streaks [11], at a reduced Landau damping rate. The dispersion of the new system of modes from PIC simulations shows that energy is shifted from SRS into BAM oscillations supported by dispersion roots of broad wave frequencies and wavenumbers. In the subsequent discussion, the term “electron-plasma wave” (EPW) is used to refer to the SRS electrostatic daughter wave in general, which includes the LW in the initial Maxwellian plasma and BAM as electron trapping modifies the distribution to a non-Maxwellian form.

Another saturation mechanism of SRS has also been proposed based on results from 1D Vlasov simulations [12] in which SRS saturation is observed to occur as the EPW breakup due to a secondary instability: Trapped particles in large-amplitude waves can give rise to modulational instability, the trapped particle instability that leads to the growth of modulations and sidebands close to the carrier waves [13]. It is well known that modulational instability leads to self-focusing in 2D and 3D [14]. When wave intensity exceeds a threshold, and for small  $k\lambda_D$ , LW intensity tends to localize in region of plasma with low density (higher index of refraction), where the enhanced ponderomotive force expels more plasma from the low-density regions and leads to long-wavelength plasma density modulations [15]. It has been shown recently that as  $k\lambda_D$  increases, the ponderomotive modulational instability becomes weaker than the electron trapped particle modulation instability (TPMI). For  $k\lambda_D = 0.33 - 0.46$ , TPMI requires a perpendicular component for the fluctuating Langmuir wave vector [16] and its nonlinear development leads to filamentation and self-focusing of the LW.

TPMI and self-focusing have been observed in two-dimensional (2D) PIC simulations [5] where the wavevector of the EPW during nonlinear SRS propagate obliquely to the laser direction, leading to diffusion of the electron velocity distribution by transverse modes. Moreover, transverse loss of trapped electrons rapidly increases as the transverse extent of

the waves narrows during self-focusing. These processes increase the Landau damping rate from its initial reduction due to electron trapping, effectively saturating SRS. In addition, electron plasma wavefront bowing is observed to occur prior to TPMI in these simulations due to nonlinear wave dispersion caused by the nonlinear frequency shift [8]. Since the nonlinear frequency shift increases with increasing wave amplitude, the wave phase velocity of EPW decreases with increasing wave amplitude. Thus, small amplitude waves at the side of the laser speckle travel faster in the direction of the laser than do large amplitude waves at the center of the laser speckle. This causes wavefronts to bend. Wavefront bowing and self-focusing, which cannot be modeled in 1D, play an important role in SRS saturation and are the focus of this work. We examine in detail here the self-localization of EPW and IAW associated with amplitude dependent frequency shift and damping.

In Sec. II, we discuss new scaling results of SRS reflectivity versus laser intensity from 2D single-speckle simulations at  $k\lambda_D = 0.34$ , where a similar sharp onset of enhanced reflectivity at an threshold laser intensity and saturation at higher intensities are obtained. The onset intensity is higher in 2D and the saturation level is lower than in 1D. Wavefront bowing and self-focusing occurs in all cases with enhanced reflectivity at intensities above the onset threshold. In Sec. III, SRS saturation is identified as a result of the combined effects of wavefront bowing and self-focusing, which initiates as the electron plasma wavefront becomes curved and rapidly terminates at the onset of self-focusing, all of which stem from incoherence and cancellation of the source terms for SRS coupling. IAW bowing is also observed in a 2D speckle simulation in the SBS dominated regime and is found to contribute to the SBS saturation. The ranges of wavelength and growth rate associated with transverse break-up of the EPW are also examined in 2D speckle simulations as well as 2D periodic systems from BGK [17] equilibrium (Sec. IV) and are compared with theory predictions [16].

## II. 2D PIC MODELING OF SRS REFLECTIVITY SCALING WITH LASER INTENSITY

A single laser speckle is a natural platform to study higher dimensional SRS because of the controlling influence of intense speckles at onset of backscatter [18]. Intense speckles are approximately diffraction limited solutions of Maxwell's equations with near field amplitudes similar to that of the laser smoothing optic, e.g. a random phase plate [19]. Single-speckle simulations are performed using the multi-dimensional (3D), massively parallel PIC code VPIC [20]. VPIC is an electromagnetic, relativistic, fully explicit, charge conserving kinetic plasma simulation code that has been used in our previous studies [5] of laser plasma interaction. The simulations are performed in 2D. In the simulations, absorbing boundary conditions are used for the fields and open boundary conditions are used for the particles. When a particle leaves a boundary, a new particle is re-injected with velocity sampled randomly from the species' initial Maxwellian distribution. A 527 nm laser enters from the left boundary following the Lindman boundary conditions [21]. A rise time of  $t\omega_{pe} = 70$  (where  $\omega_{pe}$  is the electron plasma frequency) is used for the laser intensity at the entrance to reach its maximum. The laser propagates in the  $x$  direction and at best focus its envelope is a 2D Gaussian whose intensity varies as  $\exp(-z^2/w^2)$  with a waist  $w = 2.58\mu\text{m}$ . The simulation domain has size  $100\mu\text{m} \times 14\mu\text{m}$ , a length comparable to the focal region of a  $f/4.5$  diffraction-limited beam. The simulation cell size is  $1.0\lambda_D$  to resolve small-scale electrostatic waves. The simulated plasma has temperatures  $T_e = 700\text{ eV}$  and  $T_i = 140\text{ eV}$  and a density of  $n_e/n_{cr} = 0.036$ , corresponding to a large wavenumber of  $k\lambda_D = 0.34$  for the initial EPW coupled to SRS for which wave-particle kinetic processes are important. These parameters are comparable to the plasma conditions in the Trident single-hot-spot experiments at LANL [2,11].

Similar to the scaling using 1D PIC simulations [4,5], 2D PIC simulations of SRS reflectivity vs. laser intensity at  $k\lambda_D = 0.34$  are examined. As in the 1D simulations, immobile ions are used as a neutralizing background. While ion fluctuations undoubtedly play a role in

nonlinear SRS as observed in long pulse experiments, short pulse experiments [22] and simulations have reduced dynamic ion involvement because of inertia, and we therefore choose to eliminate these dynamics in order to simplify the study of novel nonlinear electron kinetic effects. Fig. 1 shows the scaling results. The reflectivity is the time average obtained from a time interval of  $t \omega_{pe} = 20000$  in which many pulses of reflected laser light occur. Two sets of scalings are shown: the squares are from simulations using 512 particles per cell, whereas the pluses are from simulations with 128 particles per cell. The results at low intensity are more sensitive to the number of simulation particles. The convergence of SRS reflectivity with the number of particles per cell in both 1D and 2D has been examined in our earlier studies [5] in the electron trapping dominated regime: for  $k\lambda_D = 0.34$  and at intensity  $I_0 = 5.0 \times 10^{15} \text{ W/cm}^2$ , the reflectivity changes significantly in 2D simulations using 64 to 512 particles per cell but the results agree in simulations that use 512 and 750 particles per cell. However, simulations using the same parameters but at higher laser intensity require fewer simulation particles for convergence. Additional simulations at  $I_0 = 4.0 \times 10^{15} \text{ W/cm}^2$  are repeated with increasing number of particles and the time averaged SRS reflectivities from simulations with 512, 750, and 1024 particles per cell are same. Although convergence at lowest intensity  $I_0 = 3.75 \times 10^{15} \text{ W/cm}^2$  has not been examined, the simulations in Fig. 1 with intensity  $I_0 \geq 4.0 \times 10^{15} \text{ W/cm}^2$  describe the electron trapping accurately. In the subsequent discussion all results are obtained from simulations using 512 particles per cell.

First, a sharp onset of enhanced reflectivity is also observed in 2D. At laser intensity  $I_0 = 3.75 \times 10^{15} \text{ W/cm}^2$ , the reflectivity is low:  $2 \times 10^{-4}$ . However, at laser intensity  $I_0 = 4.0 \times 10^{15} \text{ W/cm}^2$ , a sharp increase in reflectivity to 0.6% results, accompanied by nonlinear processes commonly observed in 1D/2D systems, including electron trapping, a beam component in the modified electron distribution, and the resulting BAM. As the laser intensity further increases from  $I_0 = 5.0 \times 10^{15} \text{ W/cm}^2$  to  $1.0 \times 10^{16} \text{ W/cm}^2$ , a saturation level above 1% is reached. From 1D PIC simulations using the same laser and plasma conditions, the calculated reflectivity rises to the 1% level at an intensity of  $1.1 \times 10^{15} \text{ W/cm}^2$  and saturates at a few-percent level at higher intensities (see Ref. [5] for details). Compared

to the 1D results, the reflectivity scaling obtained from 2D simulations shows the same sharp onset, but occurring at a higher laser intensity than in 1D and the saturation level is lower. The lower saturation level is from new processes absent in 1D: electron plasma wavefront bowing and self-focusing. Moreover, these new processes occur in all cases for which  $I_0 \geq 4 \times 10^{15}$  W/cm<sup>2</sup> and bowing increases as EPW amplitude and laser intensity increase.

The larger onset threshold intensity in 2D stems from effects of diffraction and transverse loss of trapped electrons, as are naturally included in 2D speckle simulations. The sharp onset of SRS reflectivity with laser intensity has been examined recently in 1D systems including 3D collisional effects [23]. While the onset problem clearly involves intriguing physics, we focus here on understanding how the new nonlinear processes in 2D affect the saturation of SRS at small and large laser intensities.

### **III. SATURATION OF SRS AND SBS IN 2D SINGLE-SPECKLE SIMULATIONS: WAVEFRONT BOWING, TPMI AND SELF-FOCUSING OF PLASMA WAVES**

In order to determine the saturation mechanism for SRS, we first examine results from two simulations at weak and strong laser intensity from the set of simulations at  $k\lambda_D = 0.34$  shown in Fig. 1. In general, the backscattered light and the coupled EPW are localized on the side of the simulation domain where the laser enters into the system. As the nonlinear processes evolve, the initial Maxwellian plasma conditions are modified by electron trapping. When the first SRS pulse subsides, the subsequent SRS pulse could occur in a non-Maxwellian plasma in the presence of hot electrons, LW and BAM from the previous pulse. Thus, it is essential to first understand the saturation of the initial SRS pulses with minimal non-local effects. Fig. 2 shows results at weak intensity  $I_0 = 4.2 \times 10^{15}$  W/cm<sup>2</sup> just above the onset threshold. Of the many reflected SRS pulses during the simulation, the dynamics associated with the first two pulses are shown. The instantaneous SRS reflectivity of the first two pulses is depicted by the solid curve, whereas the time history of the EPW

energy in  $E_x$  (integrated over the transverse direction  $z$ ) is shown by the dashed curve (in arbitrary units) in Fig. 2 (a). The electrostatic energy in  $E_x$  as function of time  $t\omega_{pe}$  and spatial coordinate  $x$  during the first and second pulses is shown in (b) and (c), respectively. The SRS reflectivity reaches its peak before the  $E_x$  energy does. The results in Fig. 2 (b) and (c) suggest that the average location of the  $E_x$  envelope is at  $x \sim 10$  microns. The time required for back-scattered light to propagate from this region where it is generated to the left boundary where reflectivity is measured is  $2l(1/\omega_{pe})$ . If, as might be naively thought, SRS reflectivity were associated solely with LW amplitude, then, taking the backscattered-light transit time into account, one would expect the peak of the SRS reflectivity to occur a time interval  $2l(1/\omega_{pe})$  later than that of the  $E_x$  energy. However, the results in Fig. 2 (a) show a surprising difference: the SRS reflectivity curve reaches its peak first and begins to *decrease* as the electrostatic wave energy continues to *increase*.

We note that during both SRS pulses, the envelope of  $E_x$  exhibits spatial modulation in  $x$  with time-evolving wavelengths and an average wavelength  $\lambda_m = 2\mu\text{m}$  ( $112\lambda_D$ ). Also, during the second, stronger pulse,  $E_x$  is larger and begins to break into filaments. Figs. 2 (d) and (e) show  $E_x$  (electrostatic) and  $E_x E_y$  (where  $E_y$  is laser light) at  $t\omega_{pe} = 2510$ , corresponding to the time when the reflectivity of the first SRS pulse begins to decrease, while Figs. 2 (f) and (g) are the same quantities shown at a later time  $t\omega_{pe} = 2680$ , which corresponds to the time when the first SRS pulse is terminated. Wavefront bowing is present in  $E_x$ , as shown in Fig. 2 (d), and increases when the wave amplitude grows larger in Fig. 2 (f). Bowing results from the nonlinear dispersion associated with the nonlinear frequency shift [8] of EPW during SRS. Since the nonlinear frequency shift increases with increasing wave amplitude, the wave phase velocity decreases with increasing wave amplitude. Thus, smaller amplitude waves offset from the center of the laser speckle travel faster in  $x$  than do larger amplitude waves at the center of the speckle. As a result, the wave fronts bend. In Fig. 2 (f) the larger amplitude electrostatic waves also condense to regions of small transverse extent, a hallmark of self-focusing. The SRS reflectivity reduces as the wavefront bowing commences and terminates when self-focusing occurs. SRS saturates as a combined effect of

bowing and self-focusing, both resulting in a reduced source region for SRS generation, as shown in configuration of  $E_x E_y$  ( $\int E_x E_y dz$  is the source term [24] for SRS generation from the parametric coupling). Furthermore, transverse loss of hot electrons increases rapidly where self-focusing occurs and produces regions of small transverse extent.

These detailed processes are again examined in the simulation at higher laser intensity. Fig. 3 shows results from a 2D simulation at  $I_0 = 1.0 \times 10^{16}$  W/cm<sup>2</sup>. In Fig. 3 (a), the instantaneous SRS reflectivity during the first pulse is indicated by the solid curve. As a comparison, the time history of the  $E_x$  energy (dashed curve, arbitrary units) is overlaid. Similarly, the  $E_x$  energy is also plotted as function of time  $t\omega_{pe}$  and spatial coordinate  $x$  in Fig. 3 (b) during the first SRS pulse. As before, the average location of the  $E_x$  envelope is near  $x \sim 10$  microns and it will take the back-scattered light a time of  $21(1/\omega_{pe})$  to propagate from where it is generated to the left boundary where reflectivity is measured. Again, if SRS reflectivity were to simply track LW amplitude, then, taking the transit time into account, the peak of the SRS reflectivity curve would occur  $21(1/\omega_{pe})$  later than that of the  $E_x$  energy. However, SRS reflectivity peaks at  $660(1/\omega_{pe})$  and begins to decrease as the  $E_x$  energy continues to increase, the latter reaching its peak at  $\sim 700(1/\omega_{pe})$ .

As in the weak intensity case, spatial modulation of the  $E_x$  envelope is apparent in the region  $x = 0$  to 10 microns in Fig. 3 (b). This modulation is further shown in Figs. 3 (d) and (e), where configurations of  $E_x$  (EPW) and  $E_y$  (laser light) are displayed at  $t\omega_{pe} = 674$ , from which we estimate that spatial modulation occurs at a wavelength  $\lambda_m \sim 2\mu\text{m}$ , which is about  $112\lambda_D$ . Fourier spectral analysis of the electrostatic field  $E_x$  shows weak satellites on both sides of the main coupling wavenumber  $k\lambda_D \sim 0.34$  with a separation of  $\Delta k_m \lambda_D \sim 0.056$ . From  $\Delta k_m \lambda_D = 2\pi\lambda_D/\lambda_m$ , a modulation wavelength  $\lambda_m = 112\lambda_D$  results, which is consistent with the estimates from the spatial configurations. However, these satellites are discernible only briefly during this time interval and BAM [4,5] quickly dominate the spectrum. A similar brief appearance of spectral satellites during SRS has been shown in 1D Vlasov simulations [25], which were also replaced with stronger BAM. On the other hand, modulations from trapped particle instability have been discussed as a mechanism for SRS



saturation based on 1D Vlasov simulations [12]. We note that TPMI observed in our 2D simulations also leads to the breakup of the electrostatic field in the transverse direction, which is different from the 1D counterpart reported from the 1D Vlasov system.

To determine the origin of the reflectivity reduction, the dynamics of the SRS source term are examined. Figs. 3 (f) and (g) show the structure and time evolution of the electrostatic field  $E_x$  at  $t\omega_{pe} = 649$  and 699, respectively. The product with the laser light field  $E_x E_y$  is shown at these two times in Figs. 3 (h) and (i). Considering the time delay for the light wave to travel from the central region of the  $E_x$  envelope to the left of the simulation boundary where SRS reflectivity is measured,  $t\omega_{pe} = 649$  for  $E_x$  and  $E_x E_y$  corresponds to a time when the reflected light begins to decrease in amplitude and  $t\omega_{pe} = 699$  for  $E_x$  and  $E_x E_y$  corresponds a time when reflectivity is significantly reduced. As in the weak laser intensity case, bowing of the wave front is evident at both times shown and increases as the electrostatic field grows stronger at later time  $t\omega_{pe} = 699$ , when the fields break into filaments. (These intricate wave dynamics are clearly shown in the simulation movie accompanying this document [26], in which the EPW bowing and self-focusing evolves during the time interval  $t\omega_{pe} = 550$  to 800 of the first SRS pulse). While the modulation is most apparent near the laser entrance between  $x = 0$  and 10, the transverse breakup occurs mainly in the region  $x = 10 - 20$ . The profile of the  $E_x$  envelope as a function of  $x$  (integrated over  $z$ ) at  $t\omega_{pe} = 699$  displayed in Fig. 3 (c) further reveals that where filamentation occurs (between  $x = 10 - 20$ ), the electrostatic field energy in  $E_x$  decreases, while the energy in both the transverse component of the electrostatic field  $E_z$  and in the electron kinetic energy increase. As in the weak laser intensity case, SRS saturates from the combined effects of wavefront bowing and self-focusing. As the curvature of the wavefront increases and breaks into filaments when the wave amplitude exceeds the self-focusing instability threshold, *a large reduction of SRS arises from cancellations in the source term  $\int E_x E_y dz$  (proportional to the spatially integrated nonlinear current  $J_y \sim -en_e v_y$ , where the longitudinal field  $E_x$  contributes to  $n_e$  and the transverse field  $E_y$  drives  $v_y$ ) for SRS, which turns off the coupling eventually.* The cancellation of the source term is clearly demonstrated in Fig. 3 (k) where

transverse profiles of the laser ( $E_y$ ; green) and EPW ( $E_x$ ; red) at the stage of bowing are displayed; this cancellation becomes severe when self-focusing dominates, as shown in Fig. 3 (l). In contrast, 1D-like LW wavefronts during an early time at the onset of SRS in Fig. 3 (j) produce a coherent SRS source. Spatial modulation, as shown in Fig. 3 (d), appears in the simulations as a pre-cursor of self-focusing which dominates the wave dynamics. Although contributing to the SRS saturation, spatial modulation is likely not the main mechanism for any sudden change in reflectivity since modulation is present throughout both growing and decaying phases of the reflected pulse between  $t\omega_{pe} = 620 - 770$ . *In contrast, wavefront bowing marks the beginning of SRS saturation and self-focusing turns off the SRS reflectivity completely.*

The transverse modes associated with TPMI occur at a range of wavenumbers in simulations depending on the amplitudes of the EPW wave. Fig. 4 (a) displays the EPW  $k_z$  spectra from the strong laser intensity case. As seen from Fig. 3 (b), the electrostatic field is large in the region  $x = 0 - 20\mu\text{m}$  during the time interval  $t\omega_{pe} = 650 - 800$ . A cut of  $E_x$  at  $x = 14\mu\text{m}$  along the transverse direction  $z$  is Fourier analyzed during this time interval and the resulting  $k$ -spectrum (integrated over frequency) is shown by the solid curve in Fig. 4 (a). On the other hand, the electrostatic field is weak near  $x = 50\mu\text{m}$  during the time interval  $t\omega_{pe} = 800 - 1090$ . Similar Fourier analysis for a cut of  $E_x$  at  $x = 50\mu\text{m}$  during this time interval is shown by the dashed curve in Fig. 4 (a). Further estimates using  $E_x$  at center of speckle ( $z = 0$ ) during these times indicate that the average wave energy density  $|E_x|^2/n_e T_e \sim 0.25$  and  $0.04$  for the large and small waves, respectively. These results imply that the large-amplitude waves are unstable to long-wavelength transverse modes as the  $k$ -spectrum power indicated by the solid curve leaks at  $|k_z\lambda_D| \sim 0.05$ ; however, the small-amplitude waves are unstable to transverse modes at shorter wavelength and the  $k$ -spectrum power indicated by the dashed curve peaks at  $|k_z\lambda_D| \sim 0.1$ . The wave amplitude vs. time for the mode at  $k_z\lambda_D \sim 0.06$  from the large amplitude waves during  $t\omega_{pe} = 500 - 800$  is shown in Fig. 4 (b) with an estimated growth rate  $\gamma/\omega_{pe} \sim 0.034$ . Similarly, the wave amplitude vs. time for the mode at  $k_z\lambda_D \sim 0.12$  from the smaller amplitude waves during

$t\omega_{\text{pe}} = 800 - 1090$  is shown in Fig. 4 (c) with  $\gamma/\omega_{\text{pe}} \sim 0.007$ . These results from simulations are in qualitative agreement with implications of theory: decrease of the transverse LW diffraction coefficient with increase of LW amplitude (see Fig. 14 of Ref. [16]), combined with negative hyper-diffraction, implies that the unstable transverse mode wavenumber first increases and then decreases with increasing wave amplitude. We shall compare quantitatively the wavenumber and growth rate of the transverse modes observed in simulation and predicted by theory in Sec. IV, where the stability of a BGK equilibrium is examined in PIC simulations of a periodic system.

Let us now consider the full dynamics of the reflectivity during the entire simulation. Results from a 2D simulation for  $k\lambda_D = 0.34$  at a laser intensity  $I_0 = 5 \times 10^{15} \text{ W/cm}^2$  are shown in Fig. 5. The duration of the simulation is  $t\omega_{\text{pe}} = 20000$ , during which many reflected SRS pulses occur, as shown by the time history of the SRS instantaneous reflectivity in Fig. 5 (a). During each SRS pulse, wavefront bowing and self-focusing of the electrostatic field  $E_x$  is observed. Self-focusing of  $E_x$  during the large SRS pulse occurring near  $t\omega_{\text{pe}} = 4600$  is shown in the spatial region  $x = 10 - 20$  in Fig. 5 (d) and in region  $x = 20 - 30$  in Fig. 5 (e). The filaments in  $E_x$  also correspond to filaments in the electron density. In addition to the reduction in the SRS source term caused by wavefront bowing and self-focusing, the configuration of the  $E_x$  field during self-focusing shows regions where the transverse width is much reduced from the initial speckle width. In these narrow regions, side loss of trapped electrons, a process naturally included in 2D PIC speckle simulations, occurs at a much greater rate. Moreover, the peak regions of  $E_x$  can be offset with respect to the peak of the laser intensity, which remains at the center of the speckle. These effects further limit the growth of each SRS pulse. During the initial growth of  $E_x$ , when its wavefront is 1D-like, the local electron velocity space distribution  $(v_x, v_z)$  in Fig. 5 (b) shows a modest hot-electron tail caused by electron trapping. However, during self-focusing, when the wave field  $E_x$  is enhanced in narrow regions, the local electron velocity distribution shows an increased trapping width and density of trapped electrons, shown in Fig. 5 (c). Moreover, diffusion in transverse velocity  $v_z$  due to the transverse component of the wave vectors also occurs.

*Rapid side loss of trapped electrons and transverse velocity diffusion lead to dissipation of the wave energy and an increase in Landau damping rate in spite of strong electron trapping that reduces Landau damping initially.* The breakup of  $E_x$  into filaments is followed by the onset of side-scatter and the presence of highly oblique electrostatic waves which are no longer coupled to SRS. The nonlinear dynamics of SRS in 2D are highly complex. After the first reflected pulse, subsequent pulses grow in a system where finite amplitude, obliquely propagating electrostatic modes are present along with hot electrons.

Speckle simulations involving the ion dynamics are also examined in 2D, where TPMI and self-focusing proceed during SRS in the same manner as in the simulations using immobile ions. However, in addition to SRS, introducing mobile ions also results in SBS and an interplay between the two instabilities. In earlier work, scaling of reflectivity with ion composition is examined in 1D and 2D PIC simulations [27]. For a plasma with  $\text{He}^{2+}$  and  $\text{H}^+$  ions, large SBS reflectivity is observed when the number density of  $\text{He}^{2+}$  is between 100% to 50%, whereas comparable, lower SBS reflectivity arises when 50% to 10%  $\text{He}^{2+}$  ions are used. In these systems, SRS becomes stronger as the IAW damping of SBS increases with increasing  $\text{H}^+$  density. In Fig. 6 we show results from a 2D PIC simulation in which 50%  $\text{He}^{2+}$  and 50%  $\text{H}^+$  are used. The laser intensity is  $I_0 = 1 \times 10^{16} \text{ W/cm}^2$  and  $k\lambda_D = 0.34$ . The simulation size is  $100 \mu\text{m} \times 14 \mu\text{m}$ , with 512 particles per cell for each species and a total of 7.4 billion particles. The electrostatic energy in  $E_x$  as a function of time is displayed in Fig. 6 (a). The instantaneous reflectivity (the ratio of the outgoing to the incident laser Poynting flux integrated over the left hand boundary) from 1D (grey) and 2D (black) simulations are shown in frame (b) in which the sharp, narrow peaks are the SRS pulses embedded in broad SBS pulses in the reflected light. The running time-averaged reflectivity, grey from 1D and black from 2D simulations, is shown in frame (c). In 1D, the peak instantaneous reflectivity is higher but the reflectivity decreases rapidly in time, whereas in 2D, SBS remains strong for an extended time and the time-averaged reflectivity in 1D and 2D are comparable. The onset of SRS occurs first and is followed by SBS.

The EPW waves exhibit the same wavefront bowing, TPMI and self-focusing as shown

in Fig. 6 (d) where the  $E_x$  field from the 2D simulation at  $t\omega_{pe} = 748$  during the first SRS pulse is displayed. (During the time period of the 1st SRS pulse, the ponderomotive force of the laser light has little effect on either the ion density perturbation or the SRS reflectivity, which is clearly seen by comparing the 1st SRS pulse in Fig. 3a and Fig. 6b.) Spatial modulation of the envelope of  $E_x$  occurs near the laser entrance, similar to Fig. 3 (b). We note that the SRS dynamics with mobile ions is essentially the same as with an immobile ion background. *These results indicate that the TPPI and self-focusing discussed in this work are generic processes.*

With the growth of SRS, however, the high frequency EPW beat with IAW to produce a long-wavelength structure in the  $E_x$  field, as shown in Fig. 6 (e) as a result of the interaction of the second SRS pulse with the SBS pulse. In Figs. 6 (f) and (g), the  $k$ -spectrum (integrated over  $\omega$ ) and  $\omega - k$  spectrum obtained during the time interval of both SRS and SBS pulses ( $t\omega_{pe} = 500 - 2900$ ) are shown. The spectral components indicated are the beat, which has small negative  $k$  and gives rise to long-wavelength structures in (e), high frequency electron waves associated with SRS and BAM [4,5], and low frequency electrostatic waves associated with SBS.

Bowing of the SBS daughter IAW is also expected because of the trapped ion frequency shift [28] which increases with wave amplitude. IAW bowing is observed in a SBS-dominated, 2D speckle simulation at  $k\lambda_D = 0.34$  and a laser intensity  $I_0 = 1 \times 10^{16}$  W/cm<sup>2</sup> with 100% He<sup>2+</sup> in which IAW damping is reduced in the absence of H<sup>+</sup> ions, shown in Fig. 7. The simulation size is  $67 \mu\text{m} \times 10 \mu\text{m}$  and 512 particles per cell are used for each species (in previous convergence studies, it was found in the SBS dominated regime that the SBS reflectivity depends less sensitively on the number of simulation particles when simulations using 64 to 512 particles per cell are compared; see Ref. [5], Fig. 11). Fig. 7 shows IAW wavefront bowing at a late time  $t\omega_{pe} = 3500$  in (b) when the large SBS reflectivity begins to reduce, as shown in (a). At this time there is no observable SRS activity. Indeed, Fourier analysis of the  $E_x$  electric field shows a sharp and narrow peak in spectral power at  $k\lambda_D \sim 0.38$ , as expected for SBS. These results show that IAW wavefront bowing contributes

to the SBS saturation.

We note that the IAW also breaks up in the transverse direction in addition to exhibiting wavefront bowing, similar to the trapped electron self-focusing discussed in the SRS regime. This is evident from Fig. 7 (b), where two peaks in the amplitude of IAW offset from the laser speckle center are present in each wavefront. (The IAW dynamics are also shown in the simulation movie accompanying this document [26], in which the IAW bowing and self-focusing slowly evolves during SBS saturation in the long time interval  $t\omega_{pe} = 3000$  to 6000, in contrast with the fast-time-scale wave dynamics for the SRS case). As for the SRS saturation, IAW bowing and self-focusing lead to a reduction of SBS from cancellation of the source term  $\int E_{IAW}E_{laser}dz$ , which is seen in Fig. 7 (c) and Fig. 7 (d) where transverse profiles of the laser ( $E_y$ ; green) and IAW ( $E_x$ ; red) at the stage of bowing and self-focusing are displayed. At late times, when IAW bowing and self-focusing occur, the ion density perturbation by the ponderomotive force of the laser light is modest,  $-\delta n/n \sim 5\%$  as shown in Fig. 7 (e), and the corresponding frequency shift is small,  $(\delta\omega/\omega)_{pmf} \sim -0.002$ . On the other hand, the estimated trapped ion frequency shift [28] is much larger,  $(\delta\omega/\omega)_{TP} \sim -0.18$  (using the field amplitude  $e\phi/T_e \sim 0.6$  from the simulation). Because the two-ion-wave decay threshold depends on the damping rates of the IAW decay products [28] and their damping may not be reduced by ion trapping in the primary IAW, while the ion TPMI and subsequent self-focusing can take advantage of reduced damping from trapped ions in the primary IAW, the latter instability may have a lower threshold.

#### IV. TRAPPED ELECTRON SELF-FOCUSING SIMULATIONS USING BGK EQUILIBRIUM IN A 2D PERIODIC SYSTEM

The particular family of BGK [17] equilibria studied here may be viewed as a large-amplitude generalization of the small-amplitude traveling-wave solutions of the Vlasov-Poisson system that bifurcate from [29] linear Langmuir waves in a background (typically thermal) equilibrium plasma with distribution function  $f_0$ . They may be approximately re-

alized [8] as the fixed points of the Vlasov-Poisson system modified to include a slow linear relaxation, at rate  $\nu$ , of the electron distribution function,  $f$ , to  $f_0$ , and a small amplitude external traveling wave potential when that potential's phase velocity is chosen such that the electron density response is resonant. Alternatively, and more suitably for generating initial conditions in a PIC code, a finite amplitude harmonic traveling wave electrostatic potential,  $\phi \cos k(x - vt)$ , is used to push test particles which are replaced at rate  $\nu$  by a stochastic sampling of  $f_0$ . If the electron bounce frequency is large compared to  $\nu$ , and  $v$  is varied until resonance is obtained (i.e., until the harmonic component of the self-consistent potential matches the assumed potential), then an approximation to a BGK mode of the same family is generated with a particle representation. The less energy in the harmonics of  $k$ , the better the approximation. Also the more test particles used, the less noise in the self-consistent field, the longer the trapped particle and passing particle orbits maintain their integrity, and, hence, the better the approximation to a BGK mode.

The stability of the BGK equilibrium is examined in 2D PIC simulations of a periodic system to further understand the properties of the self-focusing instability and to compare with theory predictions at  $k_x \lambda_D = 0.35$  for an initial LW. The PIC simulation code used in this section advances the fields using scalar and vector potentials [30,31] with periodic boundary conditions for the fields and particles. First, PIC simulations in 1D are initialized with electron phase space information based on the BGK equilibrium and with immobile background ions. The simulation size is restricted to one Langmuir wavelength to isolate transverse instability (filamentation) from possible longitudinal instability. A typical 1D simulation uses 1.6 Million electrons in one wavelength of the LW and the particles and fields evolve in time until a new equilibrium is reached (the desired equilibrium does not persist long enough to see growth of the filamentation instability if one were to use fewer particles). The time duration of the 1D simulations is  $t \omega_{pe} = 1000$ . The 1D PIC equilibrium is then used to initialize 2D simulations in which 5000 electrons per cell are used. The system size in the transverse direction ( $z$ ) is varied to allow different-wavelength modes to develop from the self-focusing instability. Both 1D and 2D simulations are carried out in the wave-frame

of the LW.

In simulation units, the longitudinal electric field  $E_x$  corresponds to

$$\frac{eE_x}{m_e c \omega_{pe}} = k\lambda_D \frac{v_{th}^e}{c} \phi,$$

where  $\phi = e\Phi/T_e$  and  $E_x = k\Phi$  [16]. The simulations are performed with LW amplitudes at  $\phi = 0.15, 0.2, 0.3, 0.5$  and the dependence of the self-focusing instability on  $\phi$  and transverse wavenumber  $k_z$  is compared with theory.

Fig. 8 shows results from a 1D PIC simulation with  $\phi = 0.2$ . The initial and final electron phase space distribution are shown in Figs. 8 (a) and (b) where electron trapping is seen. We note that the trapping vortex has a small drift in  $x$  with drift speed  $\sim 0.013v_{th}^e$ , which is expected from the initial BGK solution. The trapping produces a modified tail of the velocity space distribution as indicated in (c). The  $k$ -spectrum is displayed in (d), where squares indicate the spectral components of various modes. The difference in spectral power between the fundamental  $k_x\lambda_D = 0.35$  and higher harmonics exceeds  $10^4$ , consistent with calculations from theory. At the end of the simulation, the wave energy in  $E_x$  reaches a steady state with energy decreased by  $\sim 3\%$ . Thus, the final state from the 1D PIC system is an approximate BGK equilibrium.

Results from the 2D simulations are shown in Fig. 9, in which frames (a) - (i) are from a simulation at  $\phi = 0.2$  with system length 1 (in the longitudinal direction  $x$ ) by 10 (in the transverse direction  $z$ ) Langmuir wavelengths ( $32 \times 320$  cells). The time histories for the wave energy in  $E_x$ ,  $E_z$  (on a log scale), and the electron kinetic energy are shown in (a) - (c). The electrostatic field  $E_x$  is plotted in space at initial time and at  $t\omega_{pe} = 795$  in (d) and (e); in the latter, an unstable mode in the transverse direction  $z$  is shown at the end of the linear growth phase. Later in time, shown in (f) and (g), the transverse mode evolves nonlinearly and further breaks up into smaller structures. As the transverse instability grows, the wave energy in  $E_x$  reduces, while the energy in  $E_z$  increases; at the nonlinear stage when the wave energy in  $E_z$  reaches its peak and begins to decrease, a further increase in the electron kinetic energy is observed. Compared with the velocity space distribution at initial time



(h), the final distribution (i) exhibits diffusion in velocity  $V_z$  due to the transverse modes in the system, a clear dissipative process similar to that found in speckle simulations involving self-focusing shown in Fig. 5 (c). 2D simulations of  $1 \times 40$  Langmuir wavelengths (in  $x$  and  $z$ ;  $32 \times 1280$  cells) at various  $\phi$  are carried out to examine the self-focusing instability dependence on the LW amplitude. In Fig. 9 (j), the fluctuation amplitude as a function of time for the mode at  $k_z \lambda_D \sim 0.05$  for  $\phi = 0.15$  (blue), 0.2 (green), 0.3 (orange), and 0.5 (red) are compared; the growth rate is estimated to be  $\gamma/\omega_{pe} = 0.0029, 0.0075, 0.012$ , and  $0.0147$  for the blue, green, orange, and red curve, respectively. Results indicate that the growth rate increases with increasing  $\phi$ .

For the 2D simulations examined at  $\phi = 0.2$  with variable transverse lengths to allow growth of a broad range of modes, the unstable transverse modes are found in the range  $k_z \lambda_D < 0.175$  and the fastest growing modes have wavenumbers in the range  $0.044 \leq k_z \lambda_D \leq 0.09$  with growth rates  $0.01 \geq \gamma/\omega_{pe} \geq 0.004$ . These results are in good agreement with theory [32]. On the other hand, simulations show that the growth rate of the self-focusing instability increases with increasing LW amplitude for  $\phi = 0.15 - 0.5$ , which does not appear to be entirely consistent with theory where the growth rate is shown to be the largest at an intermediate value of  $\phi$  and decreases for larger or smaller values of  $\phi$ .

## V. SUMMARY AND DISCUSSION

In this work, scaling of SRS reflectivity with laser intensity at  $k\lambda_D = 0.34$  is obtained in 2D PIC speckle simulations where a sharp onset of enhanced reflectivity at a threshold intensity and a saturated level at larger intensities are shown similar to earlier experimental results [2]. Compared with previous results from 1D PIC simulations [5], in 2D the onset occurs at a higher laser intensity and the saturation level is lower. The larger onset threshold intensity in 2D indicates the effects of diffraction and the transverse loss of trapped electrons from the sides of the 2D speckle. We have examined in detail a new saturation mechanism of SRS in 2D simulations. It is found that the combined effects of wavefront bowing and trapped

electron self-focusing of the EPW saturate SRS. Wavefront bowing initiates the saturation process, while self-focusing turns off SRS completely, both resulting from cancellations in the source term for SRS.

The wavefront bowing increases with increasing wave amplitudes (and laser intensity) and is a result of nonlinear wave dispersion [8]. In the presence of a nonlinear frequency shift, the phase velocity of EPW depends on the wave amplitude. Small-amplitude waves at the edges of a speckle travel faster than larger-amplitude waves at the center, resulting in marked curvature of the wavefronts. A nonlinear dispersion relation has been derived from Trident data (also 2D PIC simulations) [33] where the nonlinear frequency shift is measured as a function of  $k\lambda_D$  for the given laser intensity.

Self-focusing during SRS is also observed in 2D PIC simulations with full ion dynamics, where SRS and SBS interact and the saturation of SRS affects the growth of SBS. In addition, self-focusing in this  $k\lambda_D$  regime is present in multi-speckles [34] and is found in our initial 3D PIC simulations [35] shown in Fig. 10 where the dynamics of over 18 billion particles in 575 million cells are followed in time. Recently, SRS experiments were conducted at the Trident laser facility at Los Alamos where a short-pulse version of the single-hot-spot configuration was implemented [22]. It has been found [36] from 2D VPIC simulations in these high laser intensity regime ( $\geq 10^{16}$  W/cm<sup>2</sup>) that SRS (SBS) saturation is also caused by EPW (IAW) bowing and self-focusing, consistent with our findings for long laser pulse at lower intensities discussed in this work. We note that self-focusing observed in the SRS simulations *is not* related to the relativistic self-focusing instability [37] whose maximum modulational instability growth rate is a few  $\times 10^{-5}\omega_{pe}$  for the parameters of our simulations with immobile ions, which is 3 orders of magnitude smaller than that obtained from simulations (see Fig. 4). Moreover, re-run of the same simulations with a non-relativistic particle pusher show that the results are essentially the same as those from relativistic PIC in both intensity regimes,  $I_0 \leq 10^{16}$  W/cm<sup>2</sup> in this work and  $I_0 \geq 10^{16}$  W/cm<sup>2</sup> in the short-pulse cases [36].

Wavefront bowing and transverse breakup of electrostatic daughter waves are found to be generic processes associated with SRS and SBS occurring in a laser speckle. Bowing

and transverse breakup of the EPW waves are also observed in our 2D speckle simulations of SRS at other values of  $k\lambda_D = 0.19, 0.24, 0.29, 0.41$ , and  $0.45$ . In addition, we found bowing of the daughter IAW in the SBS dominated regime, which also contributes to the saturation of SBS in a laser speckle. However, since SBS evolves on the ion time scale, other ion nonlinearities, both fluid and kinetic [28], may also play roles in the saturation of SBS. More detailed analysis regarding the dominant SBS saturation mechanism in the kinetic regime will be discussed elsewhere.

The properties of the self-focusing instability are further examined in PIC simulations of a BGK equilibrium in a periodic system. It is interesting to note that the requirement of a large number of particles to maintain a long-lived BGK equilibrium is similar to the requirement for modeling accurately the electron trapping in speckle simulations of SRS. Results show that large-amplitude LW are unstable to long-wavelength transverse modes while small-amplitude LW produce shorter-wavelength unstable modes. For the LW amplitude  $\phi = 0.2$ , the unstable transverse modes have wavenumbers  $k_z\lambda_D < 0.175$  and the fastest growing modes are in the range  $0.044 \leq k_z\lambda_D \leq 0.09$  with growth rates  $0.01 \geq \gamma/\omega_{pe} \geq 0.004$ . These results from simulations are consistent with those from theory [32]. Simulations results also show that the growth rate of the self-focusing instability increases with increasing LW amplitude, with largest growth rate  $\gamma/\omega_{pe} \sim 0.0147$  found at the largest value of  $\phi$  considered,  $\phi = 0.5$ . For even larger amplitude waves in the speckle simulation with an intense laser drive, a larger growth rate  $\gamma/\omega_{pe} \sim 0.034$  is found at transverse wavenumber  $k_z\lambda_D \sim 0.06$  [Fig. 4 (b)]. However, theory predicts stability of the system to self-focusing instability at this large value of LW amplitude. Further examination is required to determine the origin of this difference. Improvements can be made in the BGK simulation, e.g., the equilibrium may be directly produced within the PIC code.

As the SRS daughter Langmuir wave amplitude grows and passes the TPMI threshold [16], the Langmuir wave, which is initially source localized to a speckle width (several microns), self-localizes in narrow channels of width a few tenths of a micron. Side loss of trapped electrons in these channels increases and Landau damping dramatically recovers

from its initial reduced value due to large electron trapping. Langmuir wave energy then decreases rapidly. Simulation results also indicate the presence of transverse wave fluctuations which leads to additional dissipation as a result of transverse electron velocity diffusion. Another manifestation of self-focusing is the development of an offset between the peak of the EPW and the laser. This also weakens the SRS coupling.

The saturation mechanism by self-localization of EPW and IAW associated with amplitude dependent frequency shift and damping discussed in this work provides key insight for developing high fidelity predictive models of SRS and SBS for ICF ignition design. In future work, the dynamics of the self-focusing instability needs to be performed in 3D simulations using a BGK equilibrium and in 3D speckle simulations to further examine its effects on SRS saturation.

# FIGURES

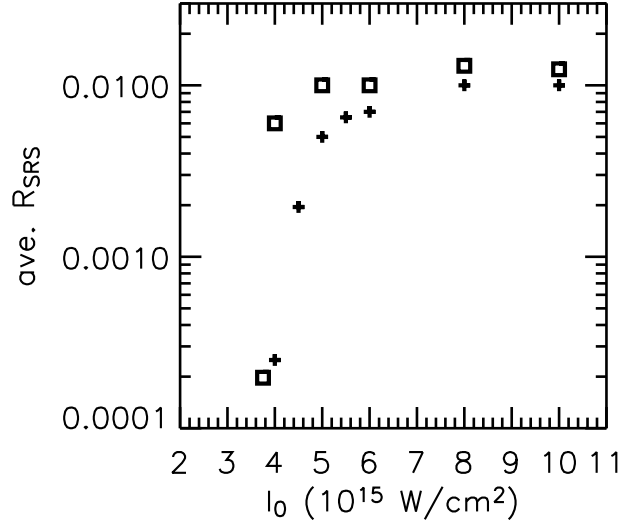


FIG. 1. 2D PIC simulations of SRS reflectivity vs. laser intensity scaling at  $k\lambda_D = 0.34$ . The reflectivity is a running time average obtained during an interval of  $t\omega_{\text{pe}} = 20000$  when many reflected laser pulses are detected. Two sets of scaling are shown: the squares are from simulations using 512 particles per cell, and the pluses are from simulations with 128 particles per cell.

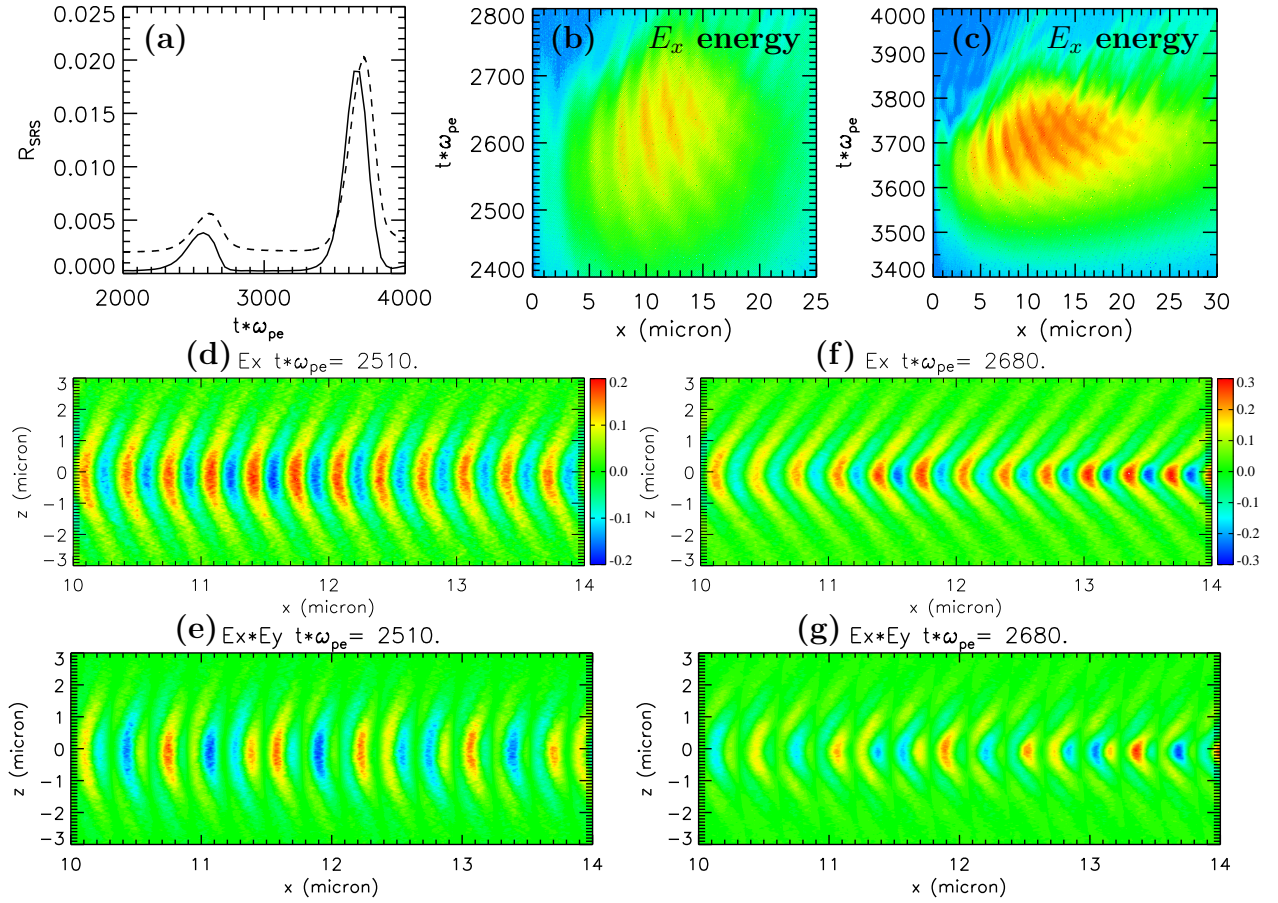


FIG. 2. (Color) Results from a 2D simulation for  $k\lambda_D = 0.34$  at laser intensity  $I_0 = 4.2 \times 10^{15}$  W/cm<sup>2</sup> (512 particles per cell; ion dynamics are not included). (a) Instantaneous SRS reflectivity (solid curve) for the first two pulses; overlaid is the time history of the electrostatic energy in  $E_x$  (dashed curve; in arbitrary units). (b) and (c) Wave energy in  $E_x$  (integrated over the transverse direction  $z$ ) as a function of time  $t\omega_{pe}$  and spatial coordinate  $x$  during the period of the first and second SRS pulse, respectively. (d) and (f) Configuration of  $E_x/\sqrt{n_e T_e}$  (EPW) at  $t\omega_{pe} = 2510$  and 2680, showing wavefront bowing and self-focusing. (e) and (g) Source terms  $E_x E_y$  (where  $E_y$  is the laser light) of SRS at these times.

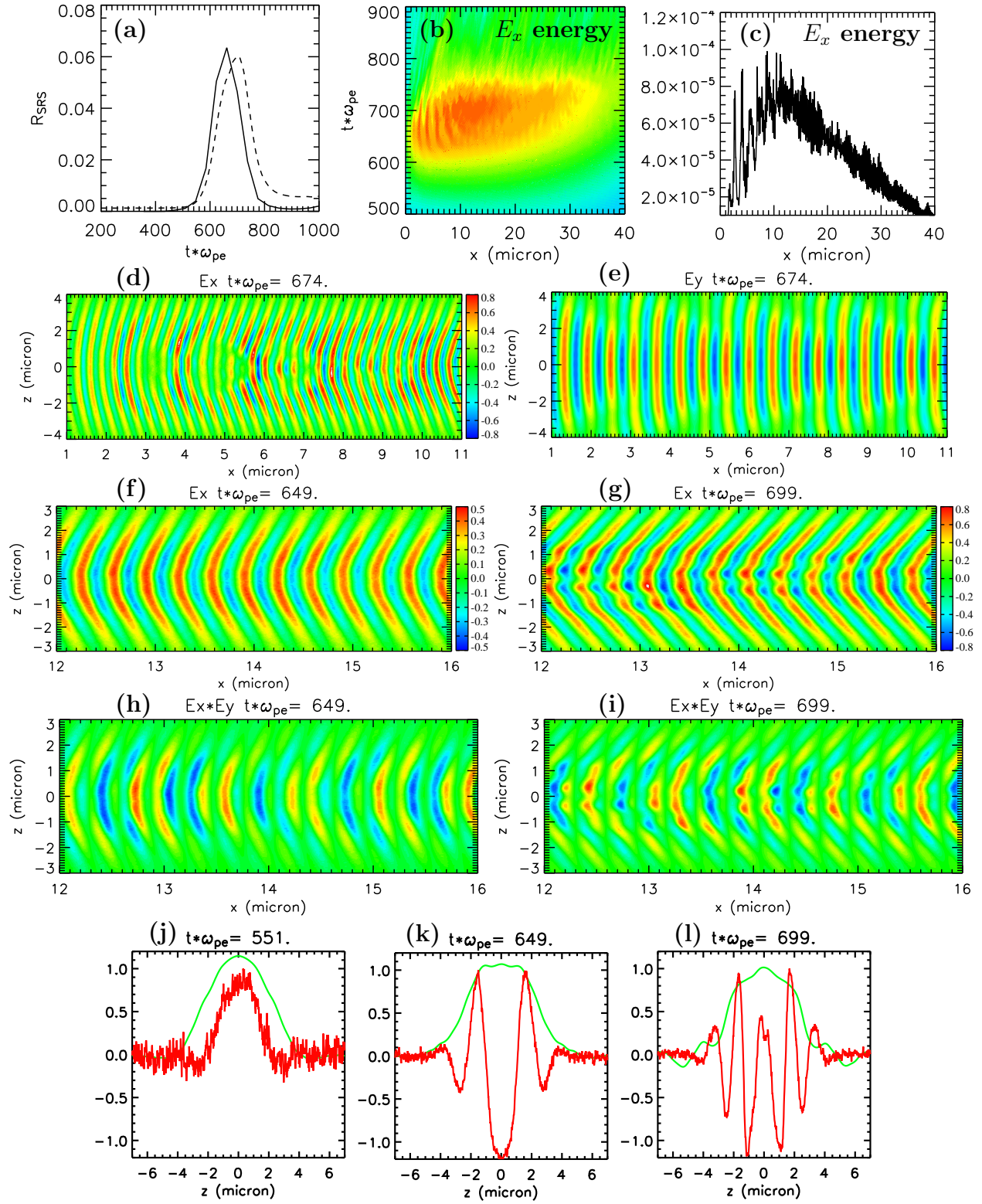


FIG. 3. (Color) Results from 2D simulation for  $k\lambda_D = 0.34$  at an intensity  $I_0 = 1 \times 10^{16}$  W/cm<sup>2</sup>. (a) Instantaneous SRS reflectivity (solid curve) of the first reflected pulse overlaid with the time history of the electrostatic  $E_x$  energy (dashed curve; in arbitrary units). (b) Energy in  $E_x$  (integrated over the transverse direction  $z$ ) as a function of time  $t\omega_{pe}$  and spatial coordinate  $x$  during the first SRS pulse. (c) Profile of energy in  $E_x$  as function of  $x$  (integrated over  $z$ ) at time  $t\omega_{pe} = 699$ . (d) and (e) Configuration of  $E_x$  (EPW) and  $E_y$  (laser light) at  $t\omega_{pe} = 674$ . (f) - (i) Configuration of  $E_x/\sqrt{n_e T_e}$  and the source terms for SRS  $E_x E_y$  at  $t\omega_{pe} = 649$  and 699, showing the effects of wavefront bowing and self-focusing in SRS saturation. (j) - (l) Transverse profiles of the laser (green) and EPW (red) during 1D-like wavefront, bowing, and self-focusing, respectively (in arb. units).



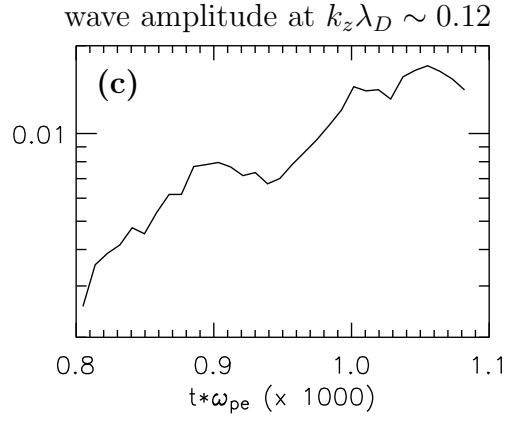
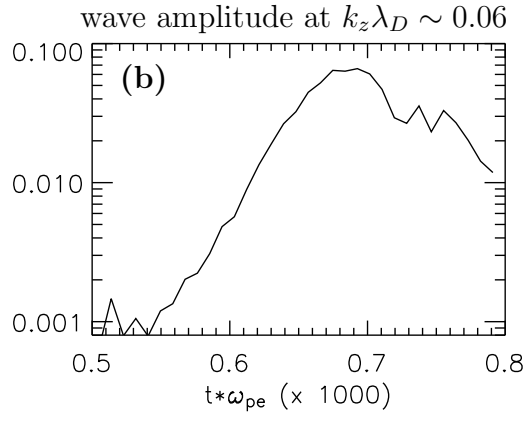
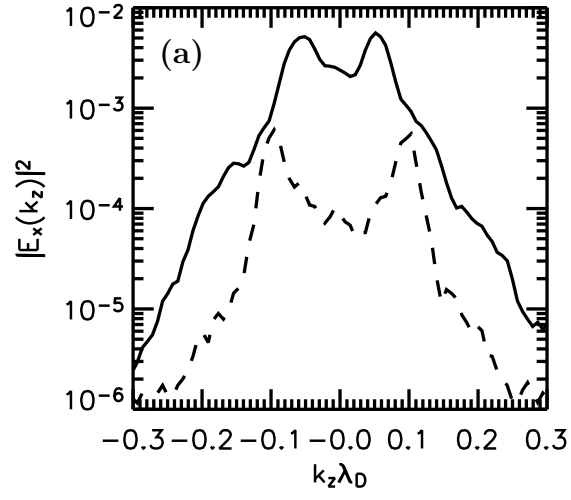


FIG. 4. Fourier analysis of transverse modes from the 2D simulation shown in Fig. 3. (a) The EPW  $k_z$  spectra (integrated over frequency) for large amplitude waves (solid curve; obtained from the electrostatic fields  $E_x$  at  $x = 14\mu\text{m}$  during  $t\omega_{\text{pe}} = 650 - 800$ ) and small amplitude waves (dashed curve; obtained at  $x = 50\mu\text{m}$  during  $t\omega_{\text{pe}} = 800 - 1090$ ); both curves are in arbitrary, but identical, units. (b) and (c) Wave amplitude vs. time for the mode at  $k_z\lambda_D \sim 0.06$  of the large amplitude waves during  $t\omega_{\text{pe}} = 500 - 800$  and for the mode at  $k_z\lambda_D \sim 0.12$  of the smaller amplitude waves during  $t\omega_{\text{pe}} = 800 - 1090$ .

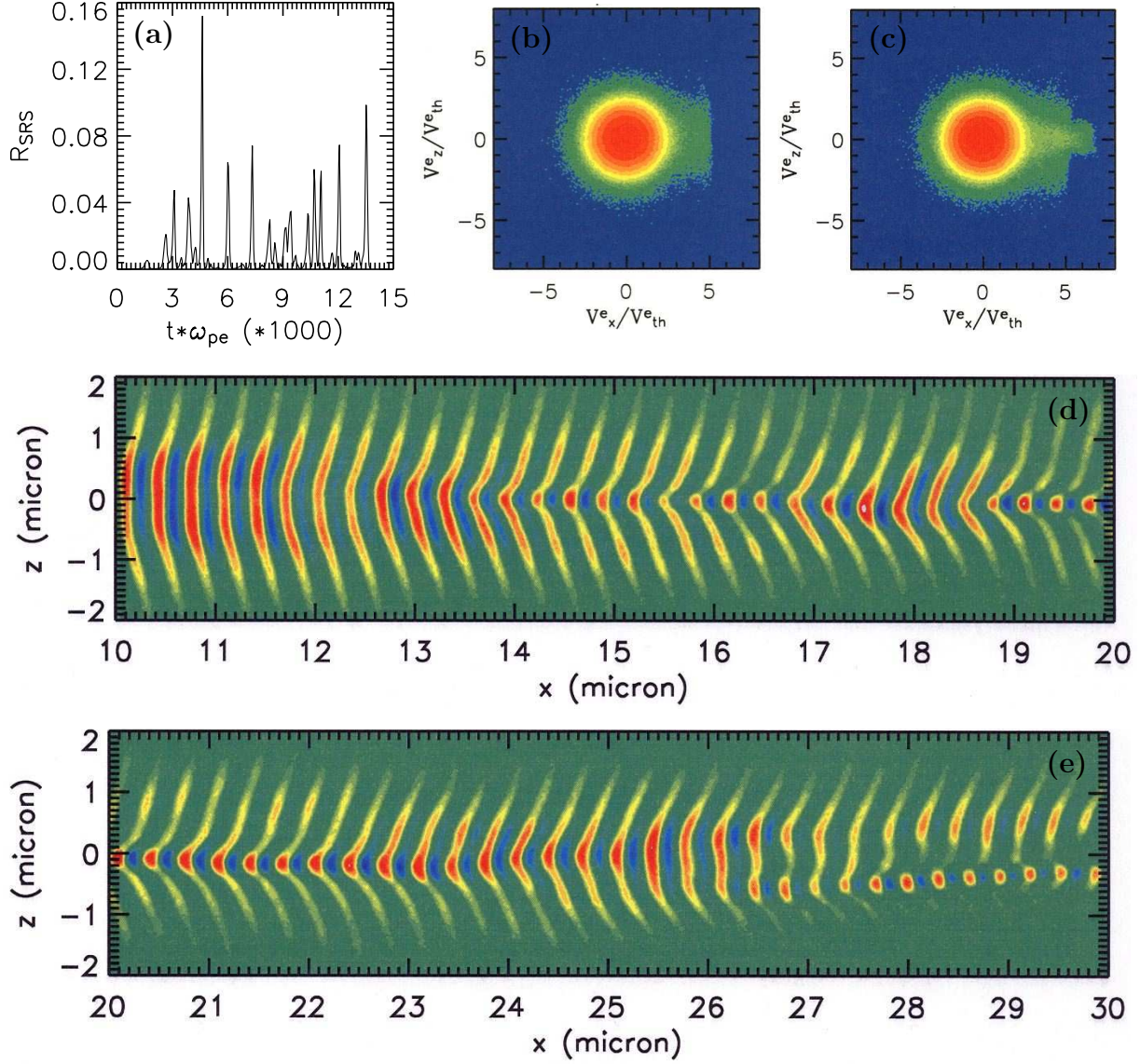


FIG. 5. (Color) Results from 2D simulation for  $k\lambda_D = 0.34$  at intensity  $I_0 = 5 \times 10^{15} \text{ W/cm}^2$ . (a) Instantaneous SRS reflectivity as a function of time showing many reflected pulses. Electron velocity space distributions ( $v_x$  and  $v_z$  are normalized to the electron thermal speed  $v_{\text{th}}^e$ ) during initial growth of  $E_x$  when it is 1D-like (b) and during strong self-focusing (c). The latter distribution indicates increased trapping width in longitudinal velocity  $v_x$  from the strong self-focused field and diffusion in velocity  $v_z$  from transverse modes. Configuration of the electrostatic field  $E_x$  in spatial region  $x = 10 - 20$  (d) and  $x = 20 - 30$  (e) showing filamentation and self-focusing during the large SRS pulse occurring near  $t\omega_{\text{pe}} = 4600$ .

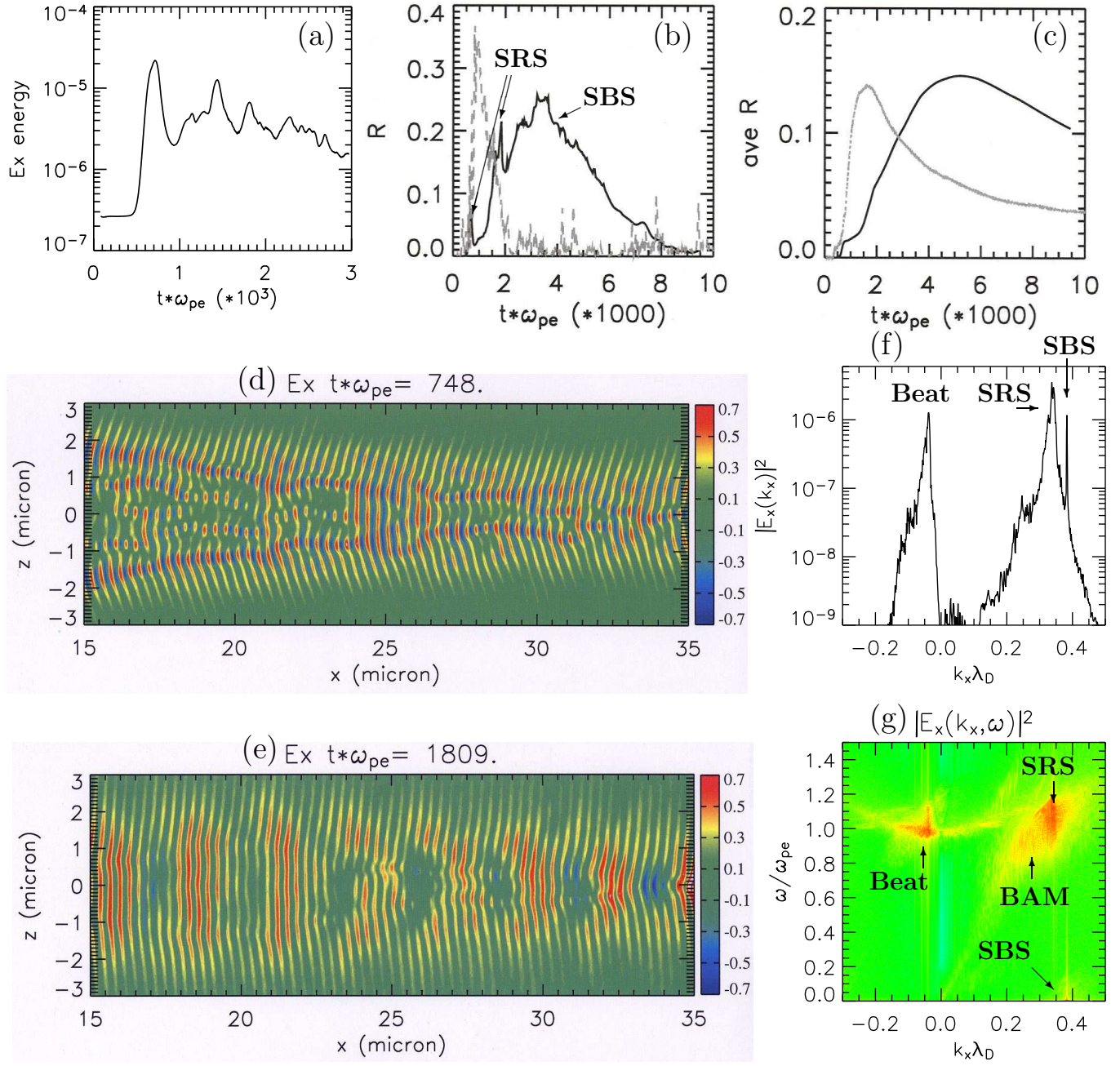


FIG. 6. (Color) Results from simulations involving the ion dynamics for  $k\lambda_D = 0.34$  with a laser intensity  $I_0 = 1 \times 10^{16}$  W/cm<sup>2</sup> (the simulation size is  $100 \mu\text{m} \times 14 \mu\text{m}$  in which 50% He<sup>2+</sup> and 50% H<sup>+</sup> are used; 512 particles per cell for each species). (a) Time history of the electrostatic energy in  $E_x$ . (b) Instantaneous reflectivity from 1D (grey) and 2D (black) simulations showing the sharp, narrow SRS pulses and broad SBS pulses in the reflected light. (c) Time-averaged reflectivity from 1D (grey) and 2D (black) simulations. Electrostatic fields  $E_x/\sqrt{n_e T_e}$  from the 2D simulation showing self-focusing (at  $t\omega_{pe} = 748$ ) during the first SRS pulse (d) and the beats (at  $t\omega_{pe} = 1809$ ) resulting from the high frequency EPW from SRS and the low frequency SBS daughter IAW (e). (f)  $k$ -spectrum ( $|E_x(\omega, k_x)|^2$  integrated over  $\omega$ ) and (g)  $\omega - k$  spectrum during the time interval  $t\omega_{pe} = 500 - 2900$  showing the spectral components of the beat, SRS, SBS, and BAM.

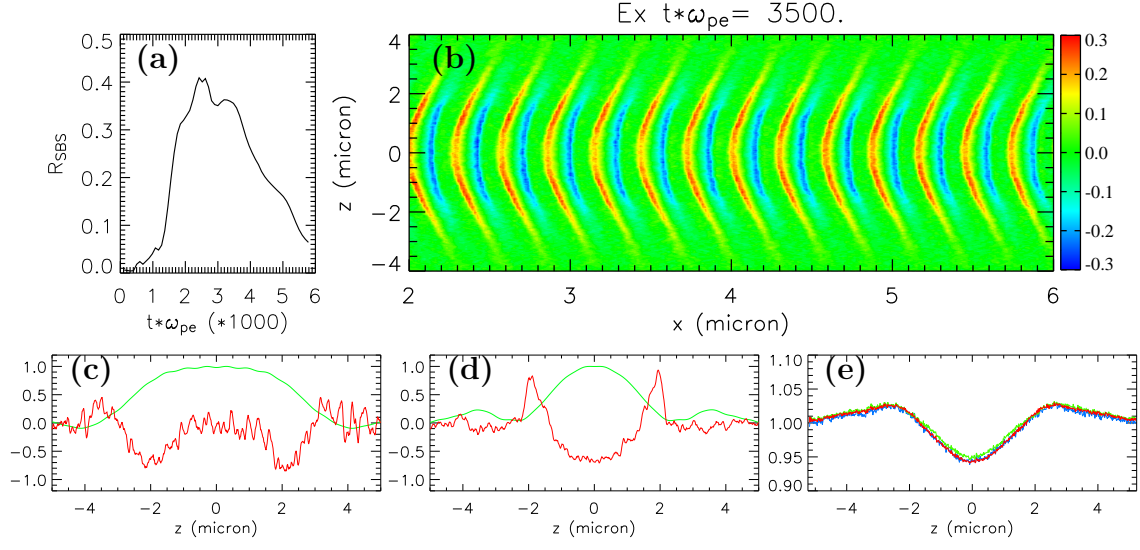


FIG. 7. (Color) Results from a SBS simulation at  $k\lambda_D = 0.34$  with a laser intensity  $I_0 = 1 \times 10^{16}$  W/cm<sup>2</sup> showing IAW wavefront bowing (b) at  $t\omega_{\text{pe}} = 3500$ , as well as transverse breakup, when the SBS reflectivity (a) begins to reduce. (c) and (d) Transverse profiles of the laser (green) and IAW (red) during bowing and self-focusing, respectively (in arb. units). (e) Transverse ion density profile showing the ion density perturbation by the ponderomotive force of the laser light during a late time when IAW bowing and self-focusing occur (results averaged over  $2\mu\text{m}$ ,  $4\mu\text{m}$ , and  $6\mu\text{m}$  in the laser direction are overlaid as indicated by the different colors).

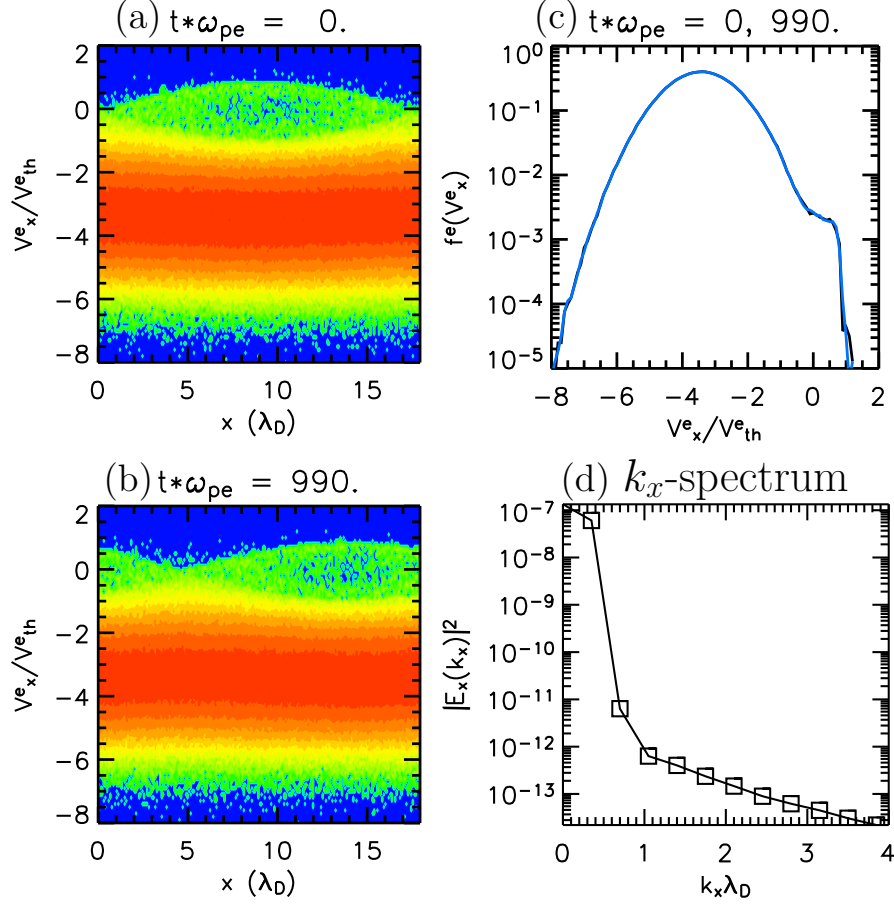


FIG. 8. (Color) Results from 1D simulation initialized with a BGK equilibrium for  $k_x\lambda_D = 0.35$  and  $\phi = 0.2$ . (a) The electron phase space distribution of at  $t\omega_{pe} = 0$  and (b) at  $t\omega_{pe} = 990$ . (c) The electron velocity space distributions at  $t\omega_{pe} = 0$  (black) and 990 (blue). (d) The  $k$ -spectrum during time  $t\omega_{pe} = 0 - 990$ .



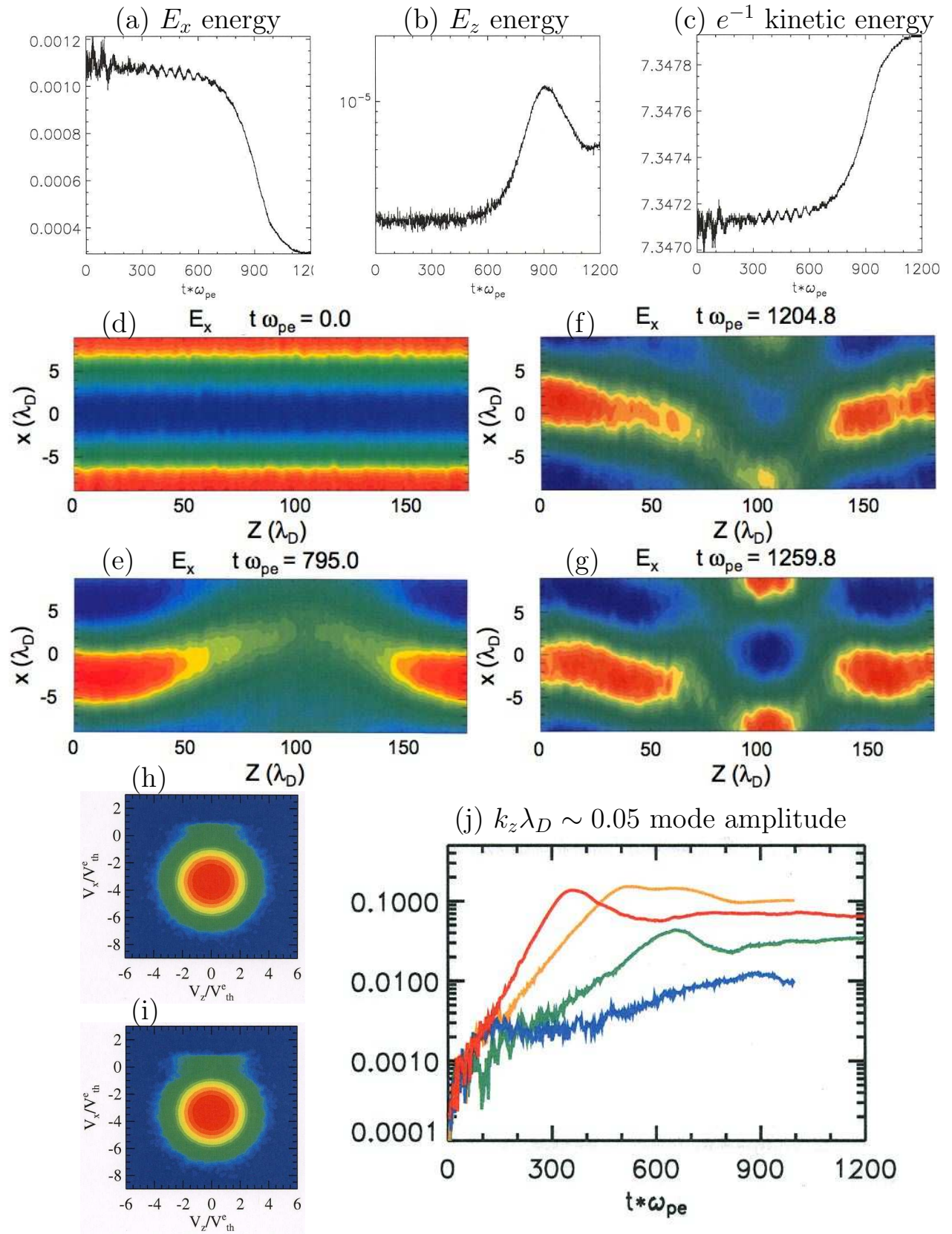




FIG. 9. (Color) Results from 2D PIC simulations using BGK equilibrium for  $k\lambda_D = 0.35$ . (a) to (i) show results from a simulation at  $\phi = 0.2$  with 1 Langmuir wavelength in  $x$  and 10 wavelengths in  $z$ . Time history of (a) longitudinal waves energy in  $E_x$ , (b) transverse wave energy in  $E_z$ , and (c) electron kinetic energy (all in the same simulation units for energy). (d) - (g) Spatial configuration of the electrostatic field  $E_x$  at  $t\omega_{pe} = 0, 795, 1205$ , and  $1260$ , in which breakup of the field  $E_x$  in the transverse direction  $z$  are shown at later times. Electron velocity space distributions at  $t\omega_{pe} = 0$  (h) and at the end of the simulation (i) when the transverse modes cause the diffusion in the transverse velocity  $V_z$ . (j) Comparison of the wave amplitude as a function of time for the mode at  $k_z\lambda_D \sim 0.05$  for  $\phi = 0.15$  (blue),  $0.2$  (green),  $0.3$  (orange), and  $0.5$  (red) in simulations with 1 Langmuir wavelength in  $x$  and 40 wavelengths in  $z$ .

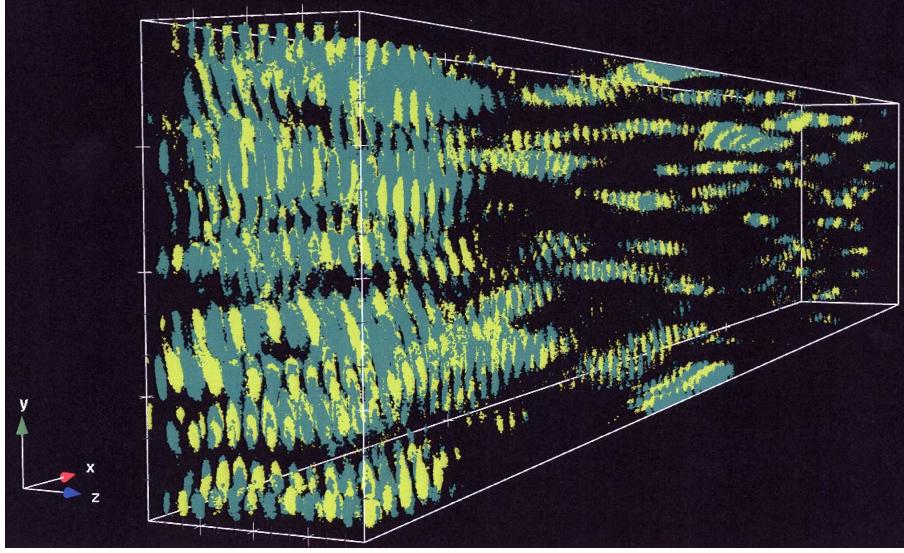


FIG. 10. (Color) 3D PIC simulation of SRS for  $I_0 = 1 \times 10^{16} \text{ W/cm}^2$  at  $k\lambda_D = 0.34$  (plasma parameters are the same as in the 2D simulations). The longitudinal EPW exhibit transverse breakup during self-focusing. The simulation follows over 18 billion particles in 575 million cells. Shown is half the simulation volume in  $z$ .

## ACKNOWLEDGMENTS

This work was performed under the auspices of the US DOE. We thank Drs. D. S. Montgomery, J. L. Kline, and J. C. Fernández for stimulating discussions, Dr. T. J. T. Kwan for his support of VPIC development, and Dr. J. Margulies for his assistance with the visualization of the 3D VPIC simulation.

## REFERENCES

- [1] J. Lindl, Phys. Plasmas, **2**, 3933 (1995).
- [2] D. S. Montgomery, J. A. Cobble, J. C. Fernandez, R. J. Focia, R. P. Johnson, N. Renard-LeGalloudec, H. A. Rose, D. A. Russell, Phys. Plasmas, **9**, 2311 (2002); D. S. Montgomery, R. J. Focia, H. A. Rose, D. A. Russell, J. A. Cobble, J. C. Fernandez, and R. P. Johnson, Phys. Rev. Lett., **87**, 155001 (2001).
- [3] In addition to the high phase velocity waves measured in the backscattered spectrum corresponding to SRS, a separate process in the backscattered spectrum at a much lower amplitude associated with the low phase velocity component, termed stimulated scattering from an electron-acoustic wave (SEAS) [2], was also identified from Trident experiments. The interpretation of the observed SEAS has been the focus of many studies: Ref. [8]; B. Afeyan, K. Won, V. Savchenko, T. W. Johnston, A. Ghizzo, P. Bertrand, Proceedings of the Third International Conference on Inertial Fusion Sciences and Applications, Monterey, CA, USA, 2003, edited by B. A. Hammel, D. D. Meyerhofer, J. Meyer-ter-Vehn, and H. Azechi (American Nuclear Soc. Inc, La Grange Park, IL, USA, 2004), p. 213-17; Ref. [25]
- [4] L. Yin, W. Daughton, B. J. Albright, B. Bezzerides, D. F. DuBois, J. M. Kindel, and H. X. Vu, Phys. Rev. E., **73**, 025401(R) (2006).
- [5] L. Yin, W. Daughton, B. J. Albright, K. J. Bowers, D. S. Montgomery, J. L. Kline, J. C. Fernández, and Q. Roper, Phys. Plasmas, **13**, 072701 (2006).
- [6] J. L. Kline, D. S. Montgomery, L. Yin, D. F. DuBois, B. J. Albright, B. Bezzerides, J. A. Cobble, E. S. Dodd, D. F. DuBois, J. C. Fernández, R. P. Johnson, J. M. Kindel, H. A. Rose, Vu, H. X., and W. S. Daughton, Phys. Plasmas, **13**, 055906 (2006).
- [7] G. J. Morales, and T. M. O’Neil, Phys. Rev. Lett., **28**, 417 (1972).
- [8] H. A. Rose, and D. A. Russell, Phys. Plasmas, **8**, 4784 (2001);

- [9] . K. Estabrook, W. L. Kruer, M. G. Haines, Phys. Fluids B, **1**, 1282 (1989).
- [10] H. X. Vu, D. F. DuBois, and B. Bezzerides, Phys. Rev. Lett., **86**, 4306 (2001); Phys. Plasmas, **9**, 1745 (2002).
- [11] J. L. Kline, D. S. Montgomery, B. Bezzerides, J. A. Cobble, D. F. DuBois, R. P. Johnson, H. A. Rose, L. Yin, and H. X. Vu, Phys. Rev. Lett., **94**, 175003 (2005).
- [12] S. Brunner, and E. J. Valeo, Phys. Rev. Lett., **93**, 145003 (2004).
- [13] W. L. Kruer, and J. M. Dawson, Phys. Rev. Lett., **23**, 838 (1969); R. L. Dewar, W. L. Kruer, and W. M. Manheimer, Phys. Rev. Lett., **28**, 215 (1972).
- [14] C. Sulem, and P. L. Sulem, *Nonlinear Schroedinger Equations: Self-Focusing and Wave Collapse* (Berlin: Springer, 1999).
- [15] V. E. Zakharov, S. L. Musher, A. M. Rubenchik, Phys. Rep., **129**, 285 (1985).
- [16] H. A. Rose, Phys. Plasmas, **12**, 12318-1 (2005).
- [17] I. B. Bernstein, J. M. Greene, and M. D. Kruskal, Physical Rev., **108**, 546 (1957).
- [18] H. A. Rose, and D. F. DuBois, Phys. Rev. Lett., **72**, 2883 (1994).
- [19] H. A. Rose, and D. F. DuBois, Phys. Fluids B, **5** 3337 (1993).
- [20] The three-dimensional, relativistic, fully electromagnetic, particle-in-cell code VPIC was developed at Los Alamos National Laboratory (LANL) by Kevin J. Bowers. VPIC is currently maintained within the Plasma Theory and Applications Section (X-1-PTA) of the Applied Science and Methods Development Group at LANL.
- [21] C. W. Neilson, and E. L. Lindman, Proc. of sixth Conf. Non. Sim of Plasmas, LLNL, LBL, Berkeley, CA, 148-151 (1973).
- [22] Kline J L, Montgomery D S, Hardin R A, Flippo K A, Shimada T, Johnson R. P., Yin L, Rose H A and Albright B J 2007 Investigation of stimulated Raman scattering

- using a short-pulse single-hot-spot at the Trident laser facility J. Phys.: Conf. Series, submitted (2007).
- [23] H. X. Vu, D. F. DuBois, and B. Bezzerides, Phys. Plasmas, **14**, 12702 (2007).
  - [24] D. A. Russell, D. F. DuBois, and H. A. Rose, Phys. Plasmas, **6**, 1294 (1999).
  - [25] D. J. Strozzi, E. A. Williams, A. B. Langdon, and A. Bers, Phys. Plasmas, **14**, 013104 (2007).
  - [26] [Web site information given here].
  - [27] L. Yin, W. Daughton, B. J. Albright, K. J. Bowers, J. L. Kline, D. S. Montgomery, and J. C. Fernández, J. Phys. IV France, **133**, 335 (2006).
  - [28] H. Ikezi, K. Schwarzenegger, A. L. Simons, Y. Onsawa, and T. Kamimura, Phys. Fluids, **21**, 239 (1978); B. I. Cohen, B. I. Cohen, B. F. Lasinski, A. B. Langdon, E. A. Williams, Phys. Plasmas, **4**, 956 (1997); B. I. Cohen, L. Divol, A. B. Langdon, and E. A. Williams, Phys. Plasmas, **12**, 052703 (2005).
  - [29] J. P. Holloway, and J. J. Dornig, Phys. Rev. A **44**, 3856 (1991).
  - [30] W. Daughton, D. Winske, L. Yin, and S. P. Gary, J. Geophys. Res., **106**, 25031 (2001).
  - [31] R. L. Morse, and C. W. Nielson, Phys. Fluids, **14**, 830 (1971).
  - [32] H. A. Rose, Bare-bones Langmuir wave model in kinetic regime, 35th Annual Anomalous Absorption Conference, Fajardo, Puerto Rico, June 26 - July 1, 2005.
  - [33] D. S. Montgomery, and J. L. Kline, paper BO1, Bull. Am. Phys. Soc. **50**, 26 (2005).
  - [34] B. J. Albright, W. Daughton, L. Yin, K. J. Bowers, J. L. Kline, D. S. Montgomery, and J. C. Fernández, J. Phys. IV France, **133**, 253 (2006).
  - [35] S. H. Batha, et al., Inertial Confinement Fusion Research at Los Alamos National Laboratory, the proceedings of The 7th symposium on current trends in fusion research,

submitted (2007).

- [36] Yin, L., B. J. Albright, K. J. Bowers, J. L. Kline, D. S. Montgomery, K. A. Flippo, and H. A. Rose, Kinetic simulations of stimulated Raman and Brillouin scattering of Trident short-pulse laser in a single-hot-spot, J. Phys.: Conf. Series, submitted (2007).
- [37] C. E. Max, J. Arons, and A. B. Langdon, Phys. Rev. Lett., **33**, 209 (1974).